PHYSICAL SCIENCES

Dimensional engineering of interlayer for efficient large-area perovskite solar cells with high stability under ISOS-L-3 aging test

Yikai Yun[1]†, Qing Chang[2]†, Jinjian Yan[3], Yuanyuan Tian[1], Sijie Jiang[1], Wenjie Wei[1], Shaoqun Li[1], Yuzheng Guo[4], Jun Yin[2], Jing Li[2], Mengyu Chen[1,5]*, Kai Huang[3,5,6]*, Cheng Li[1,5]*, Rong Zhang[3,5,6]

The utilization of low-dimensional perovskites (LDPs) as interlayers on three-dimensional (3D) perovskites has been regarded as an efficient strategy to enhance the performance of perovskite solar cells. Yet, the formation mechanism of LDPs and their impacts on the device performance remain elusive. Herein, we use dimensional engineering to facilitate the controllable growth of 1D and 2D structures on 3D perovskites. The differences of isomeric ligands in electrostatic potential distribution and steric effects for intermolecular forces contribute to different LDPs. The 1D structure facilitates charge transfer with favored channel orientation and energy level alignment. This approach enables perovskite solar modules (PSMs) using 2,2′,7,7′-tetrakis[*N*,*N*-di(4-methoxyphenyl)amino]-9,9′-spirobifluorene to achieve an efficiency of 20.20% over 10 by 10 square centimeters (cm^2) and 22.05% over 6 by 6 cm^2. In particular, a PSM (6 by 6 cm^2) using poly[bis(4-phenyl)(2,4,6-trimethylphenyl)amine] maintains an initial efficiency of ~95% after 1000 hours under the rigorous ISOS-L-3 accelerated aging tests, marking a record for the highest stability of n-i-p structure modules.

INTRODUCTION

Organic-inorganic halide perovskite (OIHP) solar cells have been tremendously developed over the past decade. Owing to the excellent photovoltaic properties of OIHP materials combined with continuous optimization (*1*, *2*), the certified power conversion efficiencies (PCEs) of perovskite solar cells (PSCs) have exceeded 26.1% (*3*, *4*). Nevertheless, because of the ionic nature and ion migration of OIHP materials (*5*, *6*), three-dimensional (3D) OIHP is susceptible to degradation from light, heat, and moisture, which restricts their large-scale applications (*7*). In particular, the abundant defects at the surface and grain boundaries (GBs) of polycrystalline perovskite films and ion migration under the external electric field (*5*) result in increased nonradiative recombination centers to deteriorate the photovoltaic performance and operational stability of PSCs (*8*–*10*).

Recently, spontaneous formation of low-dimensional perovskites (LDPs) such as 2D and 1D structures on 3D perovskites are observed by the surface treatment of the bulky ammonium salts (*11*–*16*). For instance, butylammonium (BA), benzylammonium (BzA), and phenethylammonium (PEA) have been demonstrated in the formation of stable 2D perovskites (*14*, *17*–*19*), whereas certain heterocyclic ammonium cations including thiazolium, benzimidazolium, and pyrrolium have been used for surface treatment of perovskites, resulting in 1D perovskites (*15*, *20*, *21*). These LDP structures exhibit the capability to proficiently passivate the interfacial defects between 3D perovskites and charge transport layers. However, the ambiguity in the LDP orientation presents controversial results for the heterojunction type and interfacial carrier dynamics. For example, the lateral-stacked 2D perovskites on the 3D perovskite surface may hinder the carrier extraction in vertical devices (*22*–*24*). Therefore, to address the limitations of LDP interlayers, it is necessary to establish a systematic framework governing the interactions between organic cations and octahedral inorganic layers so as to reveal the formation mechanism of different dimensional LDPs. In addition, it is highly demanded to develop an approach with minimized variables for controllable dimensionality adjustment, achieving a fair and systematic comparison of different LDP structures on the 3D perovskites.

It has been reported that the introduction of fluorine (F) atoms into organic ammonium salts can alter the surface electrostatic potential distribution of organic cations so that the introduction of the fluorinated moieties has a pronounced impact on interfacial dipole as well as the organic cations and perovskite formation energy (*25*–*28*). For example, molecular electrostatic potential distribution on intermolecular interactions is recently reported to affect the crystallization structure of Ge-based perovskite octahedra (*29*). Therefore, by varying the substitution positions of F atoms within organic ammonium cations, it is possible to influence the intermolecular interactions between the organic cations and the perovskite octahedral lattice.

Herein, by regulating the substitution position of the strong electron-withdrawing trifluoromethyl (-CF_3) group on the benzene ring, we obtain distinct LDP structures while concurrently establishing a comprehensive and equitable basis for comparison. We demonstrate that the introduction of *X*-trifluoromethyl-benzylammonium iodides (*X*-TFBzAI, including 2-TFBzAI, 3-TFBzAI, and 4-TFBzAI) enables the formation of distinct 1D and 2D structures on 3D perovskites. The formation of perovskites with different dimensionalities are due to the distinct spatial positioning of the -CF_3 in

[1]School of Electronic Science and Engineering, Xiamen University, Xiamen 361005, P. R. China. [2]Pen-Tung Sah Institute of Micro-Nano Science and Technology, Xiamen University, Xiamen 361005, China. [3]Fujian Key Laboratory of Semiconductor Materials and Applications, CI Center for OSED, Department of Physics, Xiamen University, Xiamen 361005, P. R. China. [4]School of Electrical Engineering and Automation, Wuhan University, Wuhan 430072, China. [5]Future Display Institute of Xiamen, Xiamen 361005, P. R. China. [6]Engineering Research Center of Micro-nano Optoelectronic Materials and Devices, Ministry of Education, Xiamen University, Xiamen 361005, P. R. China.
*Corresponding author. Email: mychen@xmu.edu.cn (M.C.); k_huang@xmu.edu.cn (K.H.); chengli@xmu.edu.cn (C.L.)
†These authors contributed equally to this work.

isomeric ligands and the resulting distinct electrostatic potential distribution, steric effects, and the ability of the ligands to form hydrogen bonds. In particular, the incorporation of a 1D structure with channel orientation and favored energy level alignment further facilitates the charge transfer, resulting in the devices with optimal PCEs. The 0.12-cm^2 PSCs based on the 1D interlayer achieve the PCE up to 24.19% and the 6 by 6 cm^2 (18-cm^2 active area) and 10 by 10 cm^2 (56-cm^2 active area) perovskite solar modules (PSMs) based on 2,2′,7,7′-tetrakis[*N*,*N*-di(4-methoxyphenyl)amino]-9,9′-spirobifluorene (Spiro-OMeTAD) to achieve excellent efficiencies of 22.05 and 20.20%, respectively. In addition, we conduct the aging tests of our PSMs in strict compliance with the International Summit on Organic Photovoltaic Stability (ISOS) protocols (*30*). Under rigorous accelerated aging testing conditions [ISOS-L-3 protocol, i.e., maximum power point tracking (MPPT) under AM 1.5G illumination at 85°C and 50% ± 10% relative humidity (RH)], the PSM (6 by 6 cm^2) using poly[bis(4-phenyl)(2,4,6-trimethylphenyl)amine] (PTAA) (PCE ~ 18.41%) has demonstrated a record high performance in stability (T_{95} ~ 1000 hours).

RESULTS

Ligand engineering for dimensional control of LDP structures

Figure 1A shows the schematic structures of the three ammonium cations (*X*-TFBzA$^+$) with different -CF_3 substitution positions and the corresponding electrostatic surface potential (ESP) obtained by Gaussian theoretical calculation. The different relative positions of -CF_3 and -NH_3^+ on the benzene ring result in the different electrostatic potential (φ) distributions. The maximum electrostatic potentials (φ_{max}) at the -NH_3^+ side of 2-TFBzA$^+$, 3-TFBzA$^+$, and 4-TFBzA$^+$ are evaluated as 0.235, 0.243, and 0.244, respectively. That is, the molecular polarity of 2-TFBzA$^+$ is slightly lower than 3-TFBzA$^+$ and 4-TFBzA$^+$, which may influence the interactions between the organic ligands. Considering the small differences in electrostatic potential distribution, to further reveal the influence of isomeric ammonium cations during the formation of perovskites, we grow the corresponding LDP single crystals with 2-TFBzAI, 3-TFBzAI, and 4-TFBzAI (photographs shown in figs. S2 and S3). The rotary target microfocal

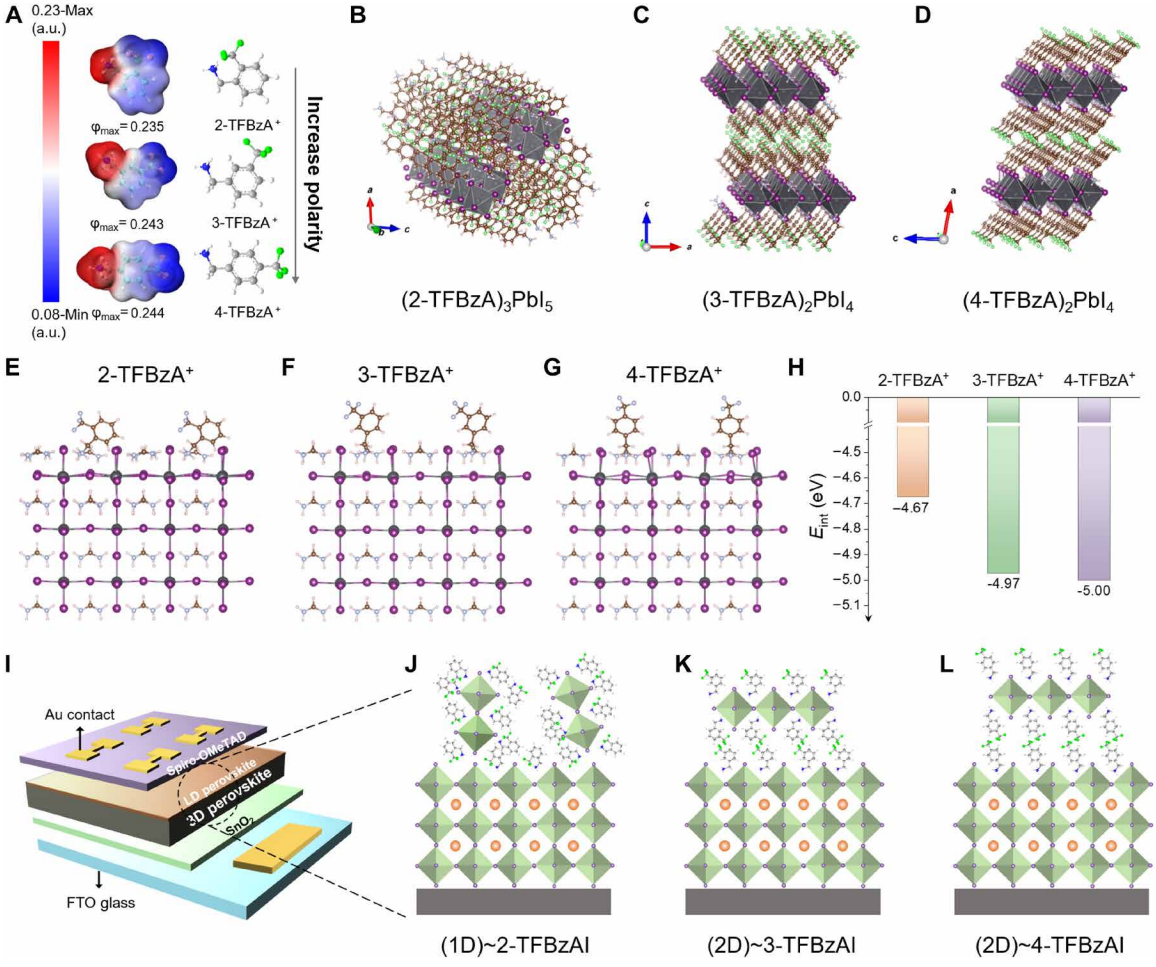

Fig. 1. Dimensional engineering mechanism and schematic diagram of passivation. (**A**) Molecular structures of three ammonium cations (2-TFBzA$^+$, 3-TFBzA$^+$, and 4-TFBzA$^+$) and the corresponding Gaussian calculated electrostatic potentials. The color bar from blue to red marks the increment of electropositivity. a.u., arbitrary units. (**B** to **D**) 1D-(2-TFBzA)$_3$PbI$_5$, 2D-(3-TFBzA)$_2$PbI$_4$, and 2D-(4-TFBzA)$_2$PbI$_4$ perovskite single-crystal structures based on 2-TFBzAI, 3-TFBzAI, and 4-TFBzAI, respectively. (**E** to **G**) DFT calculation models, with the V_A^- on the perovskite surface occupied with 2-TFBzA$^+$, 3-TFBzA$^+$, and 4-TFBzA$^+$, respectively. (**H**) E_{int} values of three ammonium ligands with the perovskite surface. (**I**) Device structure of PSCs. (**J** to **L**) Schematic stacking models of different LDP interlayers on the surfaces of 3D perovskite.

spot single-crystal diffractometer is used to analyze the lattice structure of the single crystals (lattice constants are listed in tables S1 to S3), with the corresponding structures presented in Fig. 1 (B to D). Figure 1 (C and D) depicts the formation of typical Ruddlesden-Popper (RP) 2D perovskite structures upon the introduction of 3-TFBzAI and 4-TFBzAI, respectively. These structures feature the van der Waals stackings of the inorganic monolayer of corner-sharing $[PbI_6]^{4-}$ octahedra capped with large ammonium cations, with a chemical formula of $(3\text{-TFBzA})_2PbI_4$ and $(4\text{-TFBzA})_2PbI_4$. In contrast, as shown in Fig. 1B, the introduction of 2-TFBzAI results in a strong intermolecular interaction, which causes the $[PbI_6]^{4-}$ octahedra to self-assemble into chains [1D structure, denoted as $(2\text{-TFBzA})_3PbI_5$]. Another perspective view of the lattice structure in fig. S1 further reveals that the strong intermolecular interaction can be attributed to the shorter distance between the $-CF_3$ and the $-NH_3^+$ groups in 2-TFBzA$^+$. When $-NH_3^+$ coordinates with A sites in perovskites, the electrostatic attraction between the unsaturated hydrogen on the benzene ring and the fluorine in the neighboring C—F bond facilitates a connection of adjacent function groups through C—H··F—C interactions (highlighted in red circles). This interaction leads to the formation of larger organic spacers, which causes the $[PbI_6]^{4-}$ octahedra to assemble into 1D chains instead of forming a layered (2D) structure.

To examine the interactions between different ammonium ligands and 3D perovskite surfaces, we used density functional theory (DFT) to simulate the filling of A vacancies (V_A^-) on the 3D perovskite surface by *X*-TFBzA$^+$ (Fig. 1, E to G). The corresponding interaction energies (E_{int}) between the different ammonium cations and perovskite surfaces are calculated and presented in Fig. 1H. The more negative E_{int} indicates that they are thermodynamically more favorable to the binding of molecules to the perovskite surface. 3-TFBzA$^+$ and 4-TFBzA$^+$ both exhibit a stronger tendency to bind with V_A^-, which is favored in the insertion of $-NH_3^+$ into V_A^-, to initiate the orderly packing of ligands on the perovskite surface. This may facilitate the lattice formation of lateral-stacked 2D scheme with van der Waals interaction on the 3D perovskite surface. For 2-TFBzA$^+$ with relatively weaker E_{int} to V_A^-, the insertion of $-NH_3^+$ into V_A^- accompany with the formation of hydrogen bonds (C—H··F—C) between the $-CF_3$ and the benzene ring of adjacent ligands as illustrated in fig. S1A. This leads to the formation of a distinct 1D perovskite structure on the 3D perovskite surface.

On the basis of the above analysis, we use 2-TFBzAI, 3-TFBzAI, and 4-TFBzAI to induce the formation of different dimensional LDPs on the 3D perovskite ($FA_{0.95}Cs_{0.05}PbI_3$ ~ FACs) matrix, as the passivated heterolayers to enhance both the stability and efficiency of PSCs. Figure 1I shows the schematic configuration of the PSC, with the device architecture of ITO/SnO_2/$FA_{0.95}Cs_{0.05}PbI_3$/Spiro-OMeTAD/Au. The corresponding structural schematics of self-assembled LDP/3D films treated with isomeric ammonium ligands are illustrated in Fig. 1 (J to L). Figure 1 (K and L) shows that both 3-TFBzAI and 4-TFBzAI can induce the formation of RP 2D perovskite structures parallel stacking on the 3D perovskite surface. This provides an efficient passivation of the defects at the surface and GBs but may potentially hinder the charge extraction in vertical devices. For 2-TFBzAI, as shown in Fig. 1J, the formation of chain-like 1D perovskite is facilitated on the 3D perovskite surface, which ensures both the efficient defect passivation and a conductive pathway for charge transfer at the interface.

Crystalline phase characteristics and optical properties of perovskite films

To confirm the formation of different LDPs due to the treatment of isomeric ammonium cations on 3D perovskites, we conducted the crystalline phase characterizations of the untreated perovskite film (Control) and the films treated with 2-TFBzAI, 3-TFBzAI, and 4-TFBzAI (respectively refer to 2-TFBzAI, 3-TFBzAI, and 4-TFBzAI films hereinafter).

To investigate the LDP structures, we used grazing incidence wide-angle x-ray scattering (GIWAXS). 2D GIWAXS images of Control, 2-TFBzAI, 3-TFBzAI, and 4-TFBzAI films at a grazing angle of $\alpha = 0.4°$ are shown in Fig. 2 (A to D), respectively. The Control film (Fig. 2A) shows the typical 3D perovskite diffraction rings at $[110]_c$ (q = 1 Å^{-1}) and $[220]_c$ (q = 2 Å^{-1}). For 3-TFBzAI and 4-TFBzAI films shown in Fig. 2 (C and D), respectively, the additional diffraction peaks at q ~ 0.31 and 0.68 Å^{-1} (3-TFBzAI) and q ~ 0.35 and 0.73 Å^{-1} (4-TFBzAI) are observed. This corresponds to the parallel-oriented 2D perovskite structures, indicating the formation of highly ordered 2D/3D perovskites. For the 2-TFBzAI film (Fig. 2B), a weak LDP signal (q ~ 0.27 Å^{-1}) is observed, which relates to the formation of 1D perovskites grown on the 3D perovskite surface. Moreover, the intensity of 3D perovskite diffraction rings, through the posttreatment of 2-TFBAI, is notably enhanced in all directions compared with the Control film, which confirms that the in situ secondary reaction and recrystallization process to optimize the crystallinity of 3D perovskites.

The small-angle grazing incidence x-ray diffraction (GIXRD) is adopted to provide the depth-dependent crystallographic information on the surface of LDP/3D perovskites. Figure 2 (E to H) shows the measured GIXRD patterns of Control, 2-TFBzAI, 3-TFBzAI, and 4-TFBzAI films with different incidence angles ($\omega = 0.1°$, 0.2°, 0.5°, and 1.5°) to probe the crystalline phase information from the top surface (tens of nanometers) to the inside of the films. Figure 2E shows that the Control film is a standard 3D perovskite with a diffraction peak at around q = 1 Å^{-1}. After treatment with 3-TFBzAI and 4-TFBzAI, the obvious 2D diffraction peaks can be observed in different depths, with a peak at 0.32 Å^{-1} in the 3-TFBzAI film (Fig. 2G) and a peak at 0.35 Å^{-1} in the 4-TFBzAI film (Fig. 2H). For the 2-TFBzAI film shown in Fig. 2F, an LDP peak is observed at 0.30 Å^{-1}, which corresponds to the 1D perovskite formation. This LDP signal is weaker than the ones observed in other treated films, which correlates well with the nonparallel growth of 1D perovskites on the 3D perovskite surface. At q = 0.8~1 Å^{-1}, the appearance of shoulder peaks in the data could be attributed to the presence of intermediate phases (*31*).

We then use the cross-sectional high-resolution transmission electron microscopy (HRTEM) to clearly visualize the LDP structures. We coat the perovskite films with a protective platinum layer and further process them using focused ion beam (FIB) milling. Figure 2 (I to L) illustrates the pure 3D perovskite structure of the Control sample and the presence of different LDPs on the 3D perovskite surface. We measure the interplanar spacings of perovskites in different regions, which are in good agreement with our single-crystal structural parameters (tables S1 to S3). These results provide the direct evidence for the formation of 1D and 2D perovskite on the 3D surface, which are consistent with the structural schematics of LDP/3D films in Fig. 1 (J to L).

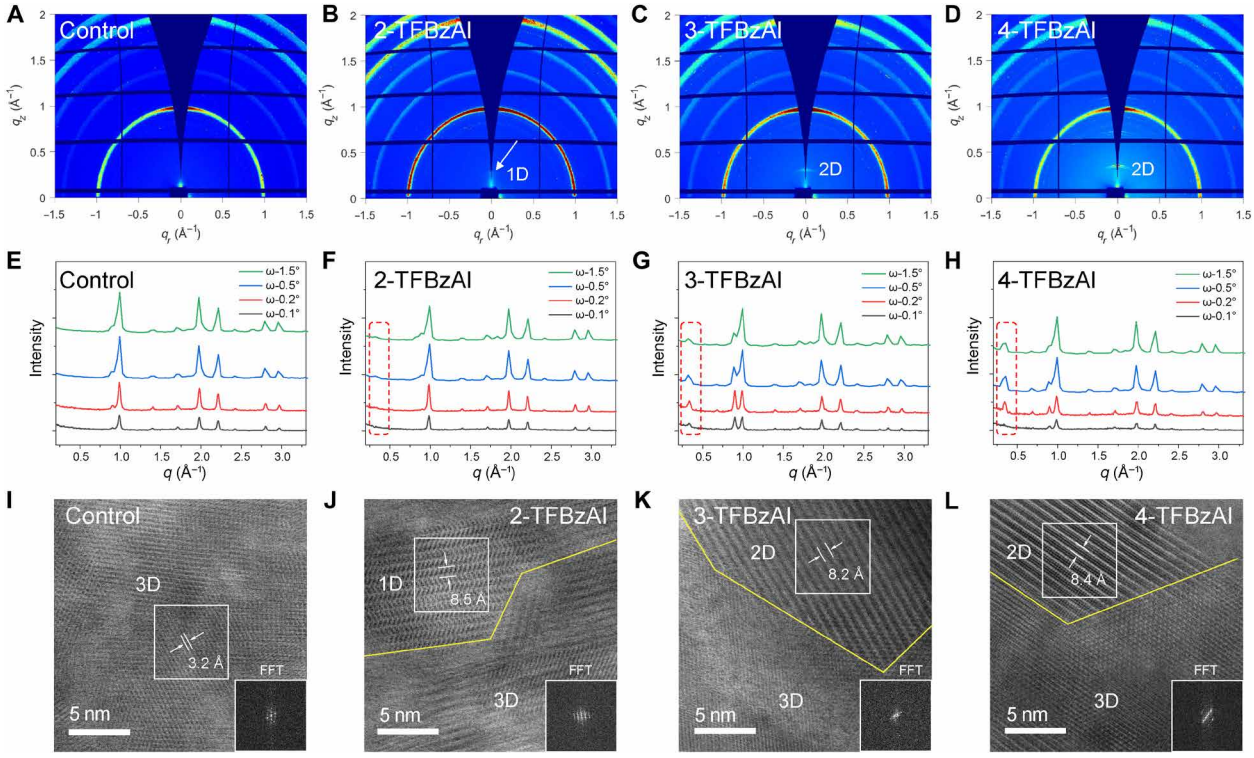

Fig. 2. Crystalline characterization of LDP interlayers. (**A** to **D**) 2D GIWAXS images of Control, 2-TFBzAI, 3-TFBzAI, and 4-TFBzAI films at a grazing angle of α = 0.4°. (**E** to **H**) GIXRD pattern of the perovskite layer without and with surface treatment. The incidence angles (ω) are 0.1°, 0.2°, 0.5°, and 1.5°. (**I** to **L**) Cross-sectional HRTEM of Control, 2-TFBzAI, 3-TFBzAI, and 4-TFBzAI films. Fast Fourier transform (FFT) is applied to the area within the white box, and the resulting FFT image is inserted.

The surface passivation properties of 1D and 2D structures on 3D perovskites are further investigated with morphology and optical characterizations. Figure 3 (A to D) compares the top-view scanning electron microscopy (SEM) images of Control, 2-TFBzAI, 3-TFBzAI, and 4-TFBzAI perovskite films. It is observed that many residual PbI_2 (small white fragments marked by yellow circles) are distributed in the GBs of perovskite polycrystals (*32*, *33*) in the Control film (Fig. 3A) and are not observed in the films treated with the three ammonium salts (Fig. 3, B to D). The reduced excess PbI_2 can be attributed to the surface reaction of ammonium ligands to form the LDP passivation layers (*28*, *34*, *35*). The x-ray diffraction (XRD) patterns (2θ scope of 5° to 55°) of different perovskite films are measured and compared in fig. S4. The characteristic peak at 12.8° corresponding to the (001) lattice of PbI_2 observed in the Control film (*36*) is substantially suppressed after the treatment of *X*-TFBzAI, which corresponds well with the morphology observations. There is no clear PbI_2 signal in the GIWAXS measurement, likely due to its primary location at the GBs with amorphous crystallinity, where its contribution to the overall diffraction pattern is minimal and easily overshadowed by the signals from the bulk perovskites. In addition, the x-ray photoelectron spectroscopy (XPS) measurement is used to analyze the interactions between *X*-TFBzAI and 3D perovskite surfaces. In the Control film (Fig. 3E), the two small peaks located at 141.58 and 136.70 eV are assigned to metallic lead (Pb^0) species, which is originated from the decomposition of PbI_2 (*37*). In all *X*-TFBzAI–treated films, the Pb^0 peaks are effectively inhibited, which further confirms that the excess PbI_2 reacts with *X*-TFBzAI and converts to LDPs. Moreover, with the comparison of the peak positions of Pb 4f between the control and treated films, we observe the slight shifts in the 3-TFBzAI and 4-TFBzAI films and a pronounced shift in the 2-TFBzAI film, indicating the formation of a stronger chemical bond (*38*, *39*). This can be attributed to the treatment of 3-TFBzAI and 4-TFBzAI to preferentially convert the 3D perovskite surface to the layered 2D structure, resulting in a high reactivity and deep penetration depth in the perovskite heterofilms (*40*). In contrast, 2-TFBzAI exhibits a weaker reactivity with the 3D perovskite surface and with a shallower distribution of the 1D passivation layer in the heterofilm, as the GIXRD analysis (Fig. 2, E to H) indicated. This may preserve a higher proportion of ammonium ligands on the surface for more effective defect passivation. The steady-state photoluminescence (PL) (Fig. 3F) and time-resolved PL (TRPL) spectroscopy (Fig. 3G) are also used to evaluate the carrier nonradiative recombination behavior of the perovskite films (*41*). After *X*-TFBzAI treatment, the PL properties of 3D perovskite films are all improved, with the 2-TFBzAI film showing the most enhanced PL intensity and prolonged PL lifetime. The average lifetime (τ_{avg}) of the 2-TFBzAI film is 1133 ns, which is notably longer than those of Control (320 ns), 3-TFBzAI (681 ns), and 4-TFBzAI (639 ns). The detailed fitted values are summarized in table S4.

Then, we consider the effect of LDP/3D heterostructures on charge transport properties in devices. We use ultraviolet (UV) photoemission spectroscopy (UPS) (Fig. 3H) and UV absorption spectrum (Fig. 3I and fig. S5) to determine the schematic energy band diagrams of the photovoltaic devices after isomeric *X*-TFBzAI treatments (Fig. 3J). Notably, the valence band maximum (E_{VBM}) of the 1D structure (−5.43 eV) is situated between the 3D perovskite

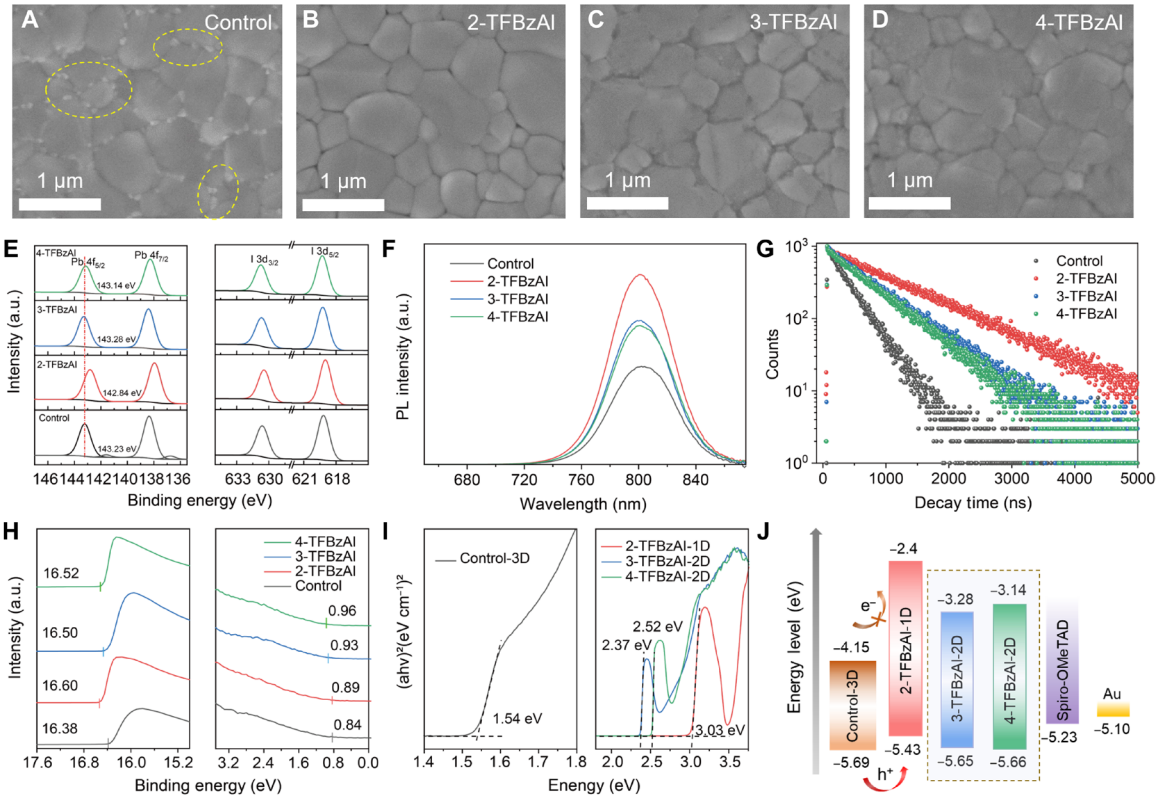

Fig. 3. Comparison of perovskite films after passivation of different LDP interlayers. (**A** to **D**) Top-view SEM images of Control, 2-TFBzAI, 3-TFBzAI, and 4-TFBzAI films. (**E**) XPS narrow-scan Pb 4f spectra, (**F**) steady-state PL spectra, (**G**) TRPL spectra, and (**H**) secondary electron cutoff and valence band regions of UPS spectra of the control 3D and LDP/3D films. (**I**) Tauc plot to analyze the optical bandgap (E^{opt}_g). (**J**) Estimated energy level alignment derived from UPS spectra based on the optimal 2-TFBzAI-1D/3D structure. The energy levels of 3-TFBzAI-2D and 4-TFBzAI-2D are also provided in the dashed box for comparison.

(−5.69 eV) and hole transport layer (HTL; Spiro-OMeTAD ~ −5.23 eV), which establishes a favorable energy level alignment to promote the hole transport. In addition, the absorption spectrum in fig. S5 shows a notable optical bandgap shift in the case of the 1D structure, which demonstrates a clear difference from the 2D structures. The 1D interlayer has a higher conduction band energy, which results in a naturally formed electron-blocking layer to reduce the leakage current between the 3D perovskite and HTL. Therefore, the 1D/3D heterostructures formed by 2-TFBzAI outperform the other 2D/3D structures in terms of both the optimal surface passivation and the favored energy shifts to facilitate the charge transfer.

In addition, we measure the TRPL with charge transport layer in fig. S6. The transient PL lifetime of the perovskites with charge transport layer shows the differences in interfacial charge transfer rates. The samples stacked with the HTL exhibit a shorter lifetime, indicating a notable carrier extraction. The introduction of three ammonium salts resulted in the even shorter lifetimes. Among them, 2-TFBzAI exhibit the shortest lifetime (64.56 ns), which can be attributed to the more favorable energy level alignment for charge transfer and the possible formation of 1D transfer channels. The detail fitted values are summarized in table S5.

Performance of PSCs based on different LDP/3D perovskites

The PSCs with a planar n-i-p device configuration of fluorine-doped tin oxide (FTO)/SnO_2/perovskite/Spiro-OMeTAD/Au are fabricated as described in Materials and Methods. The PSCs based on the perovskite film treated with 2-TFBzAI, 3-TFBzAI, and 4-TFBzAI are denoted as 2-TFBzAI-PSC, 3-TFBzAI-PSC, and 4-TFBzAI-PSC, respectively. The current density-voltage (J–V) curves of the corresponding champion devices are compared in Fig. 4A with device area of 0.12 cm^2 and under AM 1.5G illumination. The detailed performance parameters are listed in table S6. The PCE of Control-PSC (22.28%) is notably improved after X-TFBzAI treatment, with 3-TFBzAI-PSC and 4-TFBzAI-PSC reporting a PCE of 23.56 and 23.27%, respectively, and 2-TFBzAI-PSC exhibiting an optimal PCE of 24.19%. The statistical distribution plot for PCE based on 25 individual devices is summarized in Fig. 4B, which clearly shows that the 2-TFBzAI–attributed 1D/3D PSCs have superior performance compared to the other 2D/3D PSCs. The statistical comparison of various parameters of PSCs shown in fig. S7 further reveals that the optimized PCEs of the 1D/3D PSCs primarily benefited from the improvements in open-circuit voltage (V_{oc}) and fill factor (FF). This correlates well with our characterizations of the 2-TFBzAI–treated film, with suitable energy level shifts of the 1D passivation layer, to suppress the nonradiative recombination and inhibit the accumulation of interfacial charges. The incidence photon-to-electron conversion efficiency (IPCE) spectra of 2-TFBzAI-PSC and Control-PSC devices and the corresponding integrated short-circuit current density (J_{sc}) are presented in fig. S8. The integrated J_{sc} of 2-TFBzAI-PSC (24.49 mA cm^{-2}) is within 5% deviation of the value extracted from J-V curves in Fig. 4A (25.56 mA cm^{-2}), which confirms the reliability of PCE measurement.

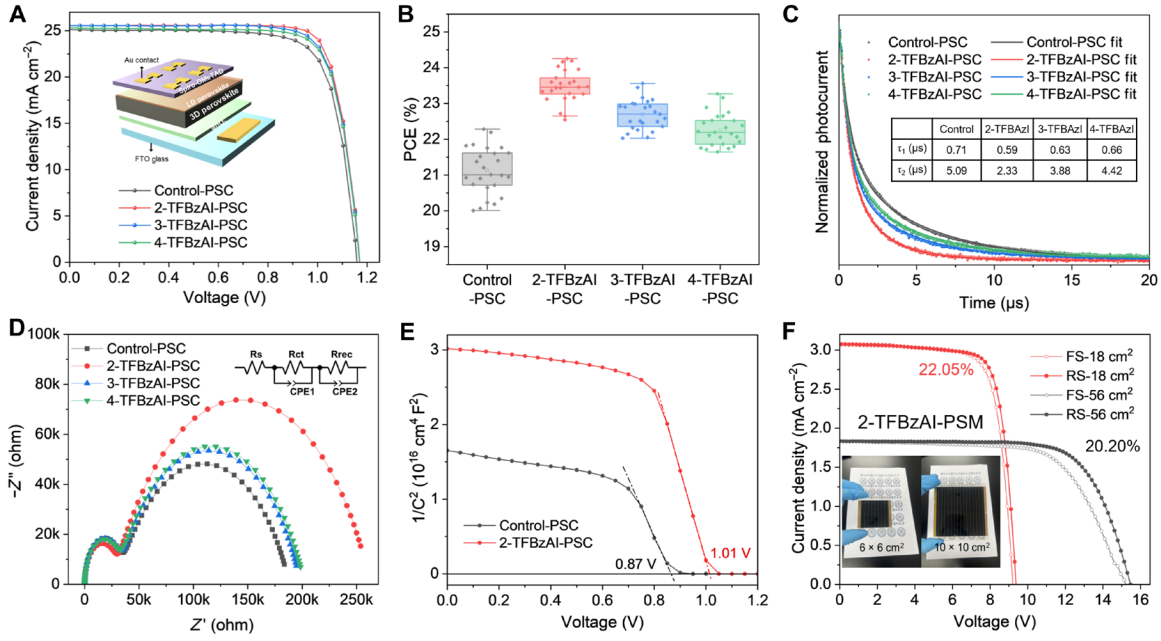

Fig. 4. Optoelectronic performance of photovoltaic devices based on LDP interlayers. (**A**) J_{sc} versus V_{oc} curves of the corresponding champion PSCs under 1-sun AM 1.5G with a scan rate of 10 mV s^{-1} using a 0.12-cm^2 mask (inset: the structure illustration of PSCs). (**B**) PCE distribution of different LDP interlayers. (**C**) TPC curves of PSCs (inset: the fitted value of decay curves). (**D**) Nyquist plots of PSCs in the dark under a bias of 0.8 V and a frequency range from 10^6 to 0.1 Hz (inset: the equivalent circuit model). (**E**) Mott-Schottky plots of Control-PSC and 2-TFBzAI-PSC. (**F**) J_{sc} versus V_{oc} curves of the 2-TFBzAI-PSMs of 18 and 56 cm^2 (inset: the photographs of PSMs).

The physical properties and charge transfer behavior of the abovementioned PSCs are further investigated. Figure 4C compares the transient photocurrent (TPC) decay curves of different devices, showing the optimized transient response after *X*-TFBzAI treatment. The inset table shows that the decay curves can be fitted with a biexponential function to obtain the fast decay constant τ_1 and the slow decay constant τ_2 (*39*). The reduced τ_1 value represents a more efficient charge transfer, and the reduced τ_2 represents a lower defect state density. Compared to the control and other treated devices, 2-TFBzAI-PSC obtains the lowest τ_1 and τ_2 values, which confirms the charge transfer channel and the optimal defect passivation of the 1D interlayer. Electrochemical impedance spectroscopy (EIS) is used to investigate the interfacial charge transfer and recombination dynamics of PSCs. Nyquist plots of different devices measured in the dark under a bias of 0.8 V and the frequency range from 10^6 to 0.1 Hz, as well as the equivalent circuit used for fitting, are shown in Fig. 4D, which clearly demonstrates two arcs. These arcs can be attributed to charge transfer resistance (R_{ct}) in the high-frequency region and the recombination resistance (R_{rec}) within the bulk perovskite layer in the low-frequency region (*42*, *43*). As indicated by the fitted values in table S7, the optimal 2TFBzAI-PSC exhibits the lowest transfer resistance (R_{ct} ~26,837 ohms) and the higher recombination resistance (R_{rec} ~235,600 ohms), corresponding to the superior charge transfer capability and enhanced defect passivation of the 1D passivation layer. Mott-Schottky analysis is used to evaluate the built-in potentials (V_{bi}). As shown in Fig. 4E, the extracted V_{bi} rises from 0.87 V (Control-PSC) to 1.01 V (2-TFBzAI-PSC). These measurements show that the 1D/3D-based 2-TFBzAI-PSC facilitates the charge transfer and suppresses the nonradiative recombination.

To validate the scalability and reliability of the 1D passivation layer, we fabricated the large-area PSMs. As illustrated in the schematic diagram of the PSM preparation process shown in fig. S10, the subcells are separated and connected by straight and smooth P1~P4 scribing lines. Because of the P2 scribing process, sidewall damage occurs within the perovskite layer, consequently to accelerate the aging of PSMs under operational conditions. Therefore, it is crucial to passivate the perovskite film after P2 scribing. The 2-TFBzAI treatment after the P2 scraping process simultaneously forms a 1D/3D heterogeneous passivation layer on both the surface and sidewalls of the delineated perovskite subcells. Compared to Control-PSM, the introduction of 2-TFBzAI has notably enhanced the performance of PSM, with the PCE of 6 by 6 cm^2 (18-cm^2 active area) and 10 by 10 cm^2 (56-cm^2 active area) modules increasing from 18.40 to 20.20% and 21.09 to 22.05%, respectively. The optimal *J*-*V* curves of the 2-TFBzAI-PSM are shown in Fig. 4F, which includes photographs of the minimodules (6 by 6 cm^2 and 10 by 10 cm^2). The detailed performance parameters are listed in table S8. Figure S11 illustrates the detailed photographs of the minimodules (6 by 6 cm^2 and 10 by 10 cm^2).

Electrical, optical, and thermal stability of perovskite films and photovoltaic devices

Ion migration is considered as one of the essential factors leading to poor stability of perovskite photovoltaic devices (*6*). To explore the effect of LDP/3D perovskites on material stability under the stresses of external electric and optical fields, we used PL imaging microscopy to in situ study the ion-related behavior of different perovskite films (*44*, *45*). Figure 5 (A and B) illustrates the ion migration images of the Control and 2-TFBzAI films with the parallel electrodes

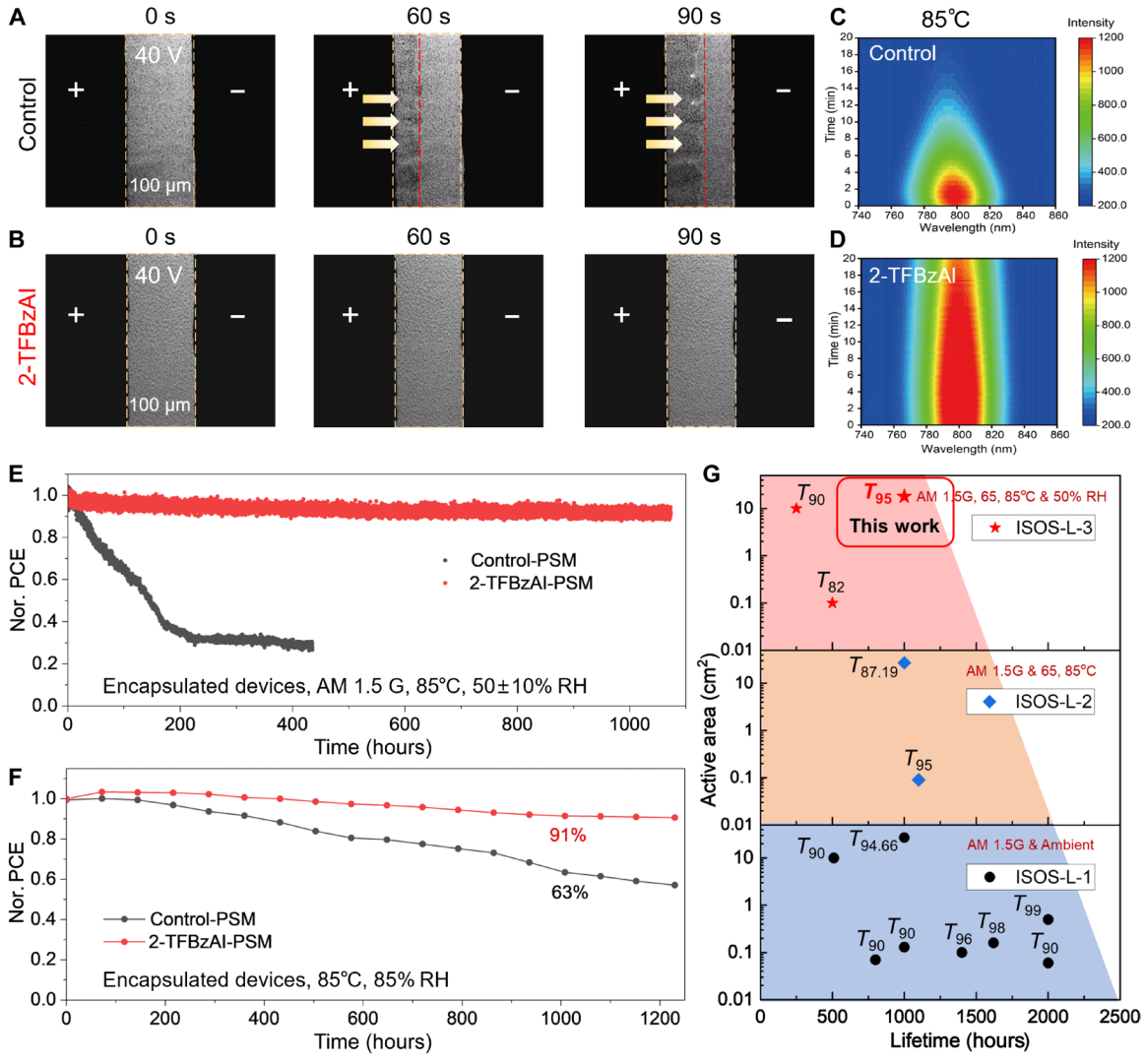

Fig. 5. Electrical, optical, and thermal stability of perovskite films and devices based on the 1D interlayer. Time-dependent microscopic PL images of (**A**) Control and (**B**) 2-TFBzAI–treated perovskite films under external bias. The polarity of the external electric field is marked by the "+" and "−" symbols. The perovskite samples are excited by a ~470-nm light source under a constant bias (40 V). The channel length is 100 μm. In situ PL spectra of (**C**) Control and (**D**) 2-TFBzAI–treated perovskite films aging at 85°C in N_2 atmosphere; the color scale bar represents the luminous intensity. (**E**) Operational stability of the encapsulated PSMs under MPPT, AM 1.5G, continuous illumination (100 mW cm^{-2}), 85°C, and 50% ± 10% RH (ISOS-L-3); the initial PCEs were 18.41% for 2-TFBzAI-PSM and 16.96% for Control-PSM. (**F**) Long-term stability of the encapsulated Control-PSM and 2-TFBzAI-PSM in the dark at 85°C and 85% RH (ISOS-D-3); the initial PCEs were 17.80% for 2-TFBzAI-PSM and 16.83% for Control-PSM. (**G**) Statistical chart of our device to the other high-efficiency n-i-p–type PSCs reported in recent years, in the comparisons of aging condition, device area, and lifetime.

deposited on the top surface. Under a constant bias (40 V) applied across the electrodes, the PL quenching process can be clearly observed in the Control film (the moving front is highlighted by red dashed line). In contrast, the 2-TFBzAI film exhibits a much stable PL behavior, and no sign of ion migration–related degradation can be observed after a continuous 40-V bias for 90 s. The ion migration images of 3-TFBzAI and 4-TFBzAI films under the same bias and stressing time are shown in fig. S12, showing that the ion migration is also efficiently inhibited. In our previous works, we have proposed that the PL quenching of perovskite films under external bias is associated with the ion migration, and these migrating ions are primarily dominated by iodine vacancies (V_i^+) (*39*, *46*, *47*). In addition, further investigations are conducted with DFT simulations for the calculation of electronic density of states, aiming to elucidate the impact of defects and *X*-TFBzAI passivation on the electronic states in perovskite. The results in fig. S13 reveal that the presence of methylammonium vacancies induces defect-associated impurity energy levels in the perovskite structure, resulting in a descent of the Fermi level. The defect states manifest as hole trap states near the VBM, contributing to the degradation of the optoelectronic properties of the perovskite. As shown in fig. S14, the filling of cationic vacancies by *X*-TFBzA$^+$ mitigates the defect states. The density of states distribution exhibits a defect-free behavior, and the Fermi level is restored to the VBM. That is, *X*-TFBzAI can effectively passivate the surface defects to stabilize the lattice structure so as to mitigate the loss of I^- ions during the annealing process and chelates with the uncoordinated Pb^{2+} ions. Therefore, not only the ion migration but also the ion/defect formation can also be suppressed

with the introduction of the *X*-TFBzAI, which results in the notable improvement in stability.

The photothermal stability of perovskite films is also explored. The in situ PL spectra are measured under a 375-nm laser pumping and 85°C to observe the degradation process of the Control and 2-TFBzAI films. As shown in Fig. 5 (C and D), the PL intensity of the Control film is decreased notably in 20 min, whereas the 2-TFBzAI film maintains a relatively stable fluorescence intensity, indicating that the self-assembled 1D/3D structure efficiently mitigates the substantial degradation of the perovskite film. Furthermore, the introduction of -CF_3 can bring better hydrophobicity, improving the perovskites stability. As shown in fig. S15, the water contact angles of perovskite films are notably increased after *X*-TFBzAI treatment.

The practical applications of photovoltaic devices should be exposed under outdoor harsh environmental conditions. Therefore, only the rigid and high-intensive aging tests can truly manifest the reliability and practical value of the PSCs (*48*). We notice that the metastability of PSCs is a complicated phenomenon in daily applications as an efficiency recovery process may occur during the diurnal cycle, with the reversibility mechanism still under debate (*49*, *50*). Considering the laboratory conditions and the accelerating degradation with both temperature and light stressing, we used the ISOS-L-3 protocol to evaluate the stability of PSCs, which is now recognized as a reliable and rigorous test. In addition, considering the defects states are inevitably increased in the PSCs with larger device area, it is necessary to conduct the accelerated aging tests in the larger devices or in PSMs. We conduct the aging tests of PSMs (6 by 6 cm^2) in strict compliance with existing ISOS stability protocols (*30*). We use PTAA instead of Spiro-OMeTAD to avoid the instability factors caused by the HTL (*51*–*53*). The relevant *J*-*V* curves and photovoltaic parameters of PSMs with PTAA as the transport layer before and after aging under different ISOS protocols are in figs. S16 and S17 and table S9. In Fig. 5E, we verified the stability under harsh operating conditions using MPPT under continuous AM 1.5G illumination at 85°C with 50% ± 10% RH (ISOS-L-3 protocol). The 2-TFBzAI-PSM maintains 95% of the initial efficiency of after 1000 hours, which is much longer than that of the Control-PSM (rapid degradation within 200 hours). In addition, fig. S18 presents the photographs of aging PSMs under the ISOS-L-3 protocol. The Control-PSM shows the signs of degradation after aging, whereas the 2-TFBzAI-PSM does not exhibit a noticeable degradation. The extraordinary operational stability of 2-TFBzAI-PSM confirms that the 1D passivation layer not only effectively inhibits the vertical ion migration in PSCs but also alleviates the sidewall defects of PSMs and inhibits the transverse ion migration at the scribing site. The hydrothermal stability is further tracked in an aging furnace of 85% RH at 85°C (ISOS-D-3 protocol). The 2-TFBzAI-PSM shows excellent stability after 1000 hours, maintaining 91% of the initial PCE, outperforming the Control-PSM (63%) in Fig. 5F.

Figure 5G compares the aging conditions, lifetimes, and device areas of our device to the other reported high-efficiency, high-stability n-i-p–type PSCs published in recent years. It can be observed that the aging tests of most devices are conducted with small device area (below 1 cm^2) and in the gentle ISOS-L-1 level, whereas the cases with accelerated aging tests under the ISOS-L-3 level are still quite rare. Our 2-TFBzAI-1D/3D PSM obtains the most prolonged lifetimes in the severe ISOS-L-3 aging test category with 18-cm^2 active area. To the best of our knowledge, it is the most stable operated n-i-p–type PSMs with the largest device area ever reported, which firmly substantiates the commercial viability of the PSMs processed with our method. The detailed information about the recently published high-performance n-i-p PSCs is summarized in table S10.

DISCUSSION

This work presents a straightforward dimensional engineering approach to obtain the controllable LDP/3D structures. It further elucidates the impact of distinct LDP structures on the surface passivation and charge carrier transport properties in PSCs. Ultimately, the high-efficiency solar cells and large-area PSMs are realized based on the optimal 2-TFBzAI-1D. In the rigorous ISOS-L-3 accelerated aging tests conducted on PSMs, a record-high operational stability of n-i-p–type PSCs is achieved. Our work not only reveals the in-depth insights about the formation and functions of the LDP/3D heterostructures in PSCs but also provides a readily available strategy to notably facilitate both the efficiency and stability of large PSMs, which substantiates the commercialization path of perovskite photovoltaic products.

MATERIALS AND METHODS

Materials

Formamidinium iodide (FAI), cesium iodide (CsI), methylamine hydrochloride (MACl), FK 209 Co(III) TFSI salt, Spiro-OMeTAD, and PTAA were purchased from Xi'an Polymer Light Technology Corp. Bis(trifluoromethane)sulfonimide lithium salt (Li-TFSI) (99.95%, Sigma-Aldrich), lead iodide (PbI_2), 4-*tert*-butylpyridine were purchased from TCI. A SnO_2 colloidal solution (15% in H_2O colloidal dispersion) was purchased from Alfa Aesar. 2-Trifluoromethyl-benzylamine (2-TFBzA), 3-trifluoromethyl-benzylamine (3-TFBzA), and 4-trifluoromethyl-benzylamine (4-TFBzA) were purchased from Aladdin.

Synthesis of trifluoromethyl-benzylamine hydroiodide

2-Trifluoromethyl-benzylamine hydroiodide (2-TFBzAI), 3-trifluo romethyl-benzylamine hydroiodide (3-TFBzAI), and 4-trifluo romethyl-benzylamine hydroiodide (4-TFBzAI) were synthesized by adding hydroiodic acid (1 mmol) into a solution of *X*-TFBzA (1 mmol) in ethanol (20 ml) at 0°C. After stirring for 3 hours, the solvent was removed by rotary evaporation, which were washed three times with diethyl ether and then vacuum dried at 40°C for 12 hours.

Synthesis of LDP single crystals

The crystal of $(3\text{-TFBzA})_2PbI_4$ and $(4\text{-TFBzA})_2PbI_4$ was prepared by mixing 2 mmol of PbI_2 and 4 mmol of 3-TFBzAI and 4-TFBzAI in the HI solution (10 ml, 53 wt % in water) in a 50-ml round-bottom flask. The produced red precipitates were dissolved by heating to 130°C to get a clear solution. Slowly cooling the solution resulted in the formation of crystals. PbI_2 (2 mmol) powder was dissolved in HI (25 ml, 53 wt %), and the mixture was stirred at 100°C for 10 min. 2-TFBzA (6 mmol) was added to the hot solution, and the resultant mixture was stirred at 140°C for 2 min. $(2\text{-TFBzA})_3PbI_5$ single crystals were obtained by slowly cooling the solution to room temperature.

Device fabrications

FTO glass substrates (Nippon Sheet Glass) were ultrasonically cleaned by glass detergent (1 vol % in deionized water), deionized

water, acetone, and ethanol for 15 min, in sequence. Substrates were treated with UV-ozone for 30 min to remove the last traces of organic residues. A compact SnO_2 electron transport layer on FTO is prepared by blade coating a SnO_2 colloidal dispersion and then annealed at 150°C for 30 min. For depositing of the $FA_{0.95}Cs_{0.05}PbI_3$ perovskite layer, a mixture solution [0.05 mmol of CsI, 0.95 mmol of FAI, 1.00 mmol of PbI_2, additives (20 mg of MACl), and 700 μl of *N*,*N*′-dimethylformamide and *N*-Methyl-2-pyrrolidone (NMP) (v/v = 9:1)] was spun on the as-prepared substrate at 5000 rpm for 40 s, and then 200 μl of ethyl acetate was dropped on the substrate prior the end of the process. Then, the substrate was heat treated at 150°C for 30 min. For perovskite surface treatment, *X*-TFBzAI (5 mg/ml) in isopropanol was deposited at 3000 rpm for 35 s. The Spiro-OMeTAD solution was prepared by dissolving 73 mg of Spiro-OMeTAD into 1 ml of chlorobenzene, followed by the addition of 18 μl of Li-TFSI [predissolved as a stock solution (520 mg/ml) in acetonitrile] and 29 μl of FK209 [predissolved as a stock solution (300 mg/ml) in acetonitrile] and 30 μl of 4-*tert*-butylpyridine. A 35-μl Spiro-OMeTAD solution was spun on the corresponding perovskite films at 3000 rpm for 30 s. Last, 80 nm of gold was evaporated as the back electrode to form the whole devices.

Large-area (6 by 6 cm^2 and 10 by 10 cm^2) perovskite films were fabricated using the blade-coating vacuum flash technique. A droplet of a perovskite precursor (40 μl) was introduced into the gap (~200 μm) between the blade and the substrate, followed by the lateral movement of the blade at a speed of 16 mm/s. Subsequently, the wet film was rapidly transferred to a vacuum chamber, which could be quickly pumped down from atmospheric pressure to 10 Pa within 1 min and then maintained at this pressure for 15 s. Following the vacuum flash process, the substrate was annealed at 110°C for 30 min and then at 130°C for an additional 30 min under atmospheric conditions. For the posttreatment of 2-TFBzAI, a solution of isopropanol (5 mg/ml) was spin coated at a speed of 60 mm/s, followed by 5 min of UV irradiation. Spiro-OMeTAD was deposited through spin coating at a speed of 40 m/s. For the device thermal stability test, PTAA was dissolved in chlorobenzene (20 mg/ml) and was used to replace Spiro-OMeTAD as the HTL. The active area of the PSMs (6 by 6 cm^2 and 10 by 10 cm^2) after the P1, P2-P4 laser scribing process was calculated to be 18 and 56 cm^2 respectively.

Characterizations

Chemical structures and ESP of the *X*-TFBzA$^+$ were computed using the Gaussian 09 program by the B3LYP DFT with 6-311+G (2d, p) basis set. The ESP distributions were visualized using GaussView. The surface morphologies and microstructures of the perovskite films were investigated using a field-emission scanning electron microscope (SUPRA55 Sapphire, Zeiss). The different perovskite films were tested by an x-ray diffractometer (D8 Advance) using Cu Kα radiation. The optical absorptions of the perovskite samples were measured using a UV-visible spectrophotometer (SHIMADZU UV-2600i). The steady-state PL spectra were obtained using a PL spectrometer (Edinburgh, FLS1000) under continuous illumination from a xenon lamp at 450 nm (34 mW cm^{-2}). The TRPL measurements were conducted at 790 nm using the Delta Flex Fluorescence Lifetime System (Edinburgh, FLS1000) with an excitation wavelength of 450 nm, and the excitation fluence was 10.19 nJ cm^{-2}. Both steady-state and transient PL were excited from the perovskite side and the HTL side. The EIS measurements were carried out by an electrochemical workstation [AUTOLAB (PGSTAT204)] in the dark at a bias of 0.8 V, a small excitation amplitude of 10 mV, and frequency range from 10^6 to 0.1 Hz. The measurements were controlled using the NOVA 2.1 software. The photocurrent density-voltage curves of the PSCs were measured using a solar simulator (Oriel 94023A, 300 W) and a Keithley 2400 source meter. The intensity (100 mW/cm^2) was calibrated using a standard Si solar cell (Oriel, VLSI standards). All the devices were tested under AM 1.5G sunlight (100 mW/cm^2) using a metal mask of 0.12 cm^2 with a scan rate of 10 mV/s. PL imaging microscopy was performed using a commercial microscope (FN1, Nikon). The perovskite films were excited by an optical excitation at a central wavelength of ~470 nm. The PL signal was directed onto a high-speed charge-coupled device camera (pco.pixelfly, PCO). A constant bias of 40 V was applied across the electrodes using a source meter unit (Keithley 2612B). Meanwhile, the time-dependent current was also monitored.

Single-crystal structure determination

The diffraction data of the single crystals of compounds (2-TFBzA)$_3PbI_5$, (3-TFBzA)$_2PbI_4$, and (4-TFBzA)$_2PbI_4$ are collected on an x-ray single-crystal diffractometer (Rigaku Oxford Diffraction system) using Mo Kα (λ = 0.71073 Å) at 100 K. The data are processed using Olex2. The structures are solved and refined using full-matrix least-squares based on F2 using ShelXT, ShelXL, and Shelxle in Olex2.

Cross-sectional HRTEM measurements

The perovskite thin films were coated with a protective platinum layer and further processed by FIB milling and polishing. The FIB milling/polishing process ensured a smooth cross section and thinned the sample to 100 nm. HRTEM images were taken using a spherical aberration-corrected transmission electron microscope [JEM-ARM300F2 (GRAND ARM2)], with the scale calibrated using a gold standard, operating at an acceleration voltage of 300 kV.

GIWAXS measurements

The x-ray energy used for the experiments was 10 keV, and the incidence angle is 0.4°. To ensure the accuracy of our results, we used the GIXGUI Matlab toolbox, using it to perform essential corrections on the raw GIWAXS patterns.

DFT simulation calculation method

In terms of the calculation method, a first-principles calculation based on DFT was conducted using the Vienna ab initio simulation software package. The generalized gradient approximation parameterized by Perdew-Burke-Ernzerhof was used as the exchange and correlation functional between electrons. The full crystal was represented by a 2 × 2 × 2 expansion of V_{MA} perovskite cells under periodic boundary conditions. A 20-Å vacuum layer was set vertically along the flat plate model to eliminate the interaction between adjacent plates due to periodicity. The electron wave function was expanded using a cutoff energy of 550 eV, and a Monkhorst-Pack *k*-point mesh (6 × 6 × 1) was used to sample the Brillouin zone. In the geometric optimization of the flat plate model, ion and electron convergence energies were specified as 1×10^{-4} and 1×10^{-5} eV, respectively. The conjugate gradient algorithm was used for the geometric optimization. The two molecular layers on the back of the substrate material were fixed, whereas other atoms were allowed to relax until the minimum total energy of the system was reached.

Stability testing

PSMs were encapsulated with polymer and covered with glass through a hot-pressing process at 100°C and 0.1-MPa pressure for stability testing. Detailed photographs of the encapsulated and unencapsulated PSM were shown in fig. S19. For ISOS-D-3 protocol stability testing, encapsulated PSMs were stored in a damp-heat chamber (K3600 MH100, McScience) with a setting at a temperature of 85°C and an RH of 85%. The modules were removed from the aging chamber every 72 hours and cooled to room temperature for current density-voltage (*J-V*) measurement using a solar simulator. For continuous operation (ISOS-L-3 protocol) stability measurements, the modules were placed on a plate in ambient air at 50% ± 10% RH. The underlying heating plate (the heating plate on which the test PSMs are placed) was maintained at 85°C, and a fixed bias voltage equivalent to the initial maximum power point voltage was continuously applied to the PSMs under the AM 1.5G condition without UV filters (a solar illumination LED was used with a circulating cooling system). The damp heat aging equipment and the multichannel MPPT testing system were under continuous illumination, as shown in fig. S20.

Supplementary Materials

This PDF file includes:

Figs. S1 to S21
Tables S1 to S10
References

REFERENCES AND NOTES

1. H. Min, M. Kim, S.-U. Lee, H. Kim, G. Kim, K. Choi, J. H. Lee, S. I. Seok, Efficient, stable solar cells by using inherent bandgap of α-phase formamidinium lead iodide. *Science* **366**, 749–753 (2019).
2. Q. Dong, Y. Fang, Y. Shao, P. Mulligan, J. Qiu, L. Cao, J. Huang, Electron-hole diffusion lengths > 175 μm in solution-grown $CH_3NH_3PbI_3$ single crystals. *Science* **347**, 967–970 (2015).
3. J. Park, J. Kim, H.-S. Yun, M. J. Paik, E. Noh, H. J. Mun, M. G. Kim, T. J. Shin, S. I. Seok, Controlled growth of perovskite layers with volatile alkylammonium chlorides. *Nature* **616**, 724–730 (2023).
4. NREL, Best Research-Cell Efficiency Chart, https://nrel.gov/pv/cell-efficiency.html.
5. B. Chen, P. N. Rudd, S. Yang, Y. Yuan, J. Huang, Imperfections and their passivation in halide perovskite solar cells. *Chem. Soc. Rev.* **48**, 3842–3867 (2019).
6. S. Bai, P. Da, C. Li, Z. Wang, Z. Yuan, F. Fu, M. Kawecki, X. Liu, N. Sakai, J. T.-W. Wang, S. Huettner, S. Buecheler, M. Fahlman, F. Gao, H. J. Snaith, Planar perovskite solar cells with long-term stability using ionic liquid additives. *Nature* **571**, 245–250 (2019).
7. K. Ho, M. Wei, E. H. Sargent, G. C. Walker, Grain transformation and degradation mechanism of formamidinium and cesium lead iodide perovskite under humidity and light. *ACS Energy Lett.* **6**, 934–940 (2021).
8. W. Tress, N. Marinova, T. Moehl, S. M. Zakeeruddin, M. K. Nazeeruddin, M. Grätzel, Understanding the rate-dependent J–V hysteresis, slow time component, and aging in $CH_3NH_3PbI_3$ perovskite solar cells: The role of a compensated electric field. *Energ. Environ. Sci.* **8**, 995–1004 (2015).
9. C. Eames, J. M. Frost, P. R. F. Barnes, B. C. O'Regan, A. Walsh, M. S. Islam, Ionic transport in hybrid lead iodide perovskite solar cells. *Nat. Commun.* **6**, 7497 (2015).
10. M. Abdi-Jalebi, Z. Andaji-Garmaroudi, S. Cacovich, C. Stavrakas, B. Philippe, J. M. Richter, M. Alsari, E. P. Booker, E. M. Hutter, A. J. Pearson, S. Lilliu, T. J. Savenije, H. Rensmo, G. Divitini, C. Ducati, R. H. Friend, S. D. Stranks, Maximizing and stabilizing luminescence from halide perovskites with potassium passivation. *Nature* **555**, 497–501 (2018).
11. J. Chen, Y. Yang, H. Dong, J. Li, X. Zhu, J. Xu, F. Pan, F. Yuan, J. Dai, B. Jiao, X. Hou, A. K.-Y. Jen, Z. Wu, Highly efficient and stable perovskite solar cells enabled by low-dimensional perovskitoids. *Sci. Adv.* **8**, eabk2722 (2022).
12. S. Sidhik, Y. Wang, M. De Siena, R. Asadpour, A. J. Torma, T. Terlier, K. Ho, W. Li, A. B. Puthirath, X. Shuai, A. Agrawal, B. Traore, M. Jones, R. Giridharagopal, P. M. Ajayan, J. Strzalka, D. S. Ginger, C. Katan, M. A. Alam, J. Even, M. G. Kanatzidis, A. D. Mohite, Deterministic fabrication of 3D/2D perovskite bilayer stacks for durable and efficient solar cells. *Science* **377**, 1425–1430 (2022).
13. Y. Liu, S. Akin, L. Pan, R. Uchida, N. Arora, J. V. Milić, A. Hinderhofer, F. Schreiber, A. R. Uhl, S. M. Zakeeruddin, A. Hagfeldt, M. I. Dar, M. Grätzel, Ultrahydrophobic 3D/2D fluoroarene bilayer-based water-resistant perovskite solar cells with efficiencies exceeding 22%. *Sci. Adv.* **5**, eaaw2543 (2019).
14. T. Niu, J. Lu, M.-C. Tang, D. Barrit, D.-M. Smilgies, Z. Yang, J. Li, Y. Fan, T. Luo, I. McCulloch, A. Amassian, S. Liu, K. Zhao, High performance ambient-air-stable $FAPbI_3$ perovskite solar cells with molecule-passivated Ruddlesden–Popper/3D heterostructured film. *Energ. Environ. Sci.* **11**, 3358–3366 (2018).
15. R. Chen, H. Shen, Q. Chang, Z. Tang, S. Nie, B. Chen, T. Ping, B. Wu, J. Yin, J. Li, N. Zheng, Conformal imidazolium 1D perovskite capping layer stabilized 3D perovskite films for efficient solar modules. *Adv. Sci.* **9**, 2204017 (2022).
16. Y. Cho, A. M. Soufiani, J. S. Yun, J. Kim, D. S. Lee, J. Seidel, X. Deng, M. A. Green, S. Huang, A. W. Y. Ho-Baillie, Mixed 3D–2D passivation treatment for mixed-cation lead mixed-halide perovskite solar cells for higher efficiency and better stability. *Adv. Energy Mater.* **8**, 1703392 (2018).
17. P. Chen, Y. Bai, S. Wang, M. Lyu, J.-H. Yun, L. Wang, In situ growth of 2D perovskite capping layer for stable and efficient perovskite solar cells. *Adv. Funct. Mater.* **28**, 1706923 (2018).
18. W. Li, Q. Wu, L. Lu, Y. Tian, H. Luo, Y. Yun, S. Jiang, M. Chen, C. Li, Molecular engineering for sensitive, fast and stable quasi-two-dimensional perovskite photodetectors. *J. Mater. Chem. C* **11**, 3314–3324 (2023).
19. R. Yang, R. Li, Y. Cao, Y. Wei, Y. Miao, W. L. Tan, X. Jiao, H. Chen, L. Zhang, Q. Chen, H. Zhang, W. Zou, Y. Wang, M. Yang, C. Yi, N. Wang, F. Gao, C. R. McNeill, T. Qin, J. Wang, W. Huang, Oriented quasi-2D perovskites for high performance optoelectronic devices. *Adv. Mater.* **30**, e1804771 (2018).
20. L. Gao, I. Spanopoulos, W. Ke, S. Huang, I. Hadar, L. Chen, X. Li, G. Yang, M. G. Kanatzidis, Improved environmental stability and solar cell efficiency of $(MA,FA)PbI_3$ perovskite using a wide-band-gap 1D thiazolium lead iodide capping layer strategy. *ACS Energy Lett.* **4**, 1763–1769 (2019).
21. A. F. Xu, N. Liu, F. Xie, T. Song, Y. Ma, P. Zhang, Y. Bai, Y. Li, Q. Chen, G. Xu, Promoting thermodynamic and kinetic stabilities of FA-based perovskite by an in situ bilayer structure. *Nano Lett.* **20**, 3864–3871 (2020).
22. D. Yu, F. Cao, C. Su, G. Xing, Exploring, identifying, and removing the efficiency-limiting factor of mixed-dimensional 2D/3D perovskite solar cells. *Acc. Chem. Res.* **56**, 959–970 (2023).
23. F. Wang, Q. Chang, Y. Yun, S. Liu, Y. Liu, J. Wang, Y. Fang, Z. Cheng, S. Feng, L. Yang, Y. Yang, W. Huang, T. Qin, Hole-transporting low-dimensional perovskite for enhancing photovoltaic performance. *Research* **9797053**, (2021).
24. H. Tsai, W. Nie, J.-C. Blancon, C. C. Stoumpos, R. Asadpour, B. Harutyunyan, A. J. Neukirch, R. Verduzco, J. J. Crochet, S. Tretiak, L. Pedesseau, J. Even, M. A. Alam, G. Gupta, J. Lou, P. M. Ajayan, M. J. Bedzyk, M. G. Kanatzidis, A. D. Mohite, High-efficiency two-dimensional Ruddlesden–Popper perovskite solar cells. *Nature* **536**, 312–316 (2016).
25. X. Zhao, M. L. Ball, A. Kakekhani, T. Liu, A. M. Rappe, Y.-L. Loo, A charge transfer framework that describes supramolecular interactions governing structure and properties of 2D perovskites. *Nat. Commun.* **13**, 3970 (2022).
26. R. Lin, J. Xu, M. Wei, Y. Wang, Z. Qin, Z. Liu, J. Wu, K. Xiao, B. Chen, S. M. Park, G. Chen, H. R. Atapattu, K. R. Graham, J. Xu, J. Zhu, L. Li, C. Zhang, E. H. Sargent, H. Tan, All-perovskite tandem solar cells with improved grain surface passivation. *Nature* **603**, 73–78 (2022).
27. L. Wang, Q. Zhou, Z. Zhang, W. Li, X. Wang, Q. Tian, X. Yu, T. Sun, J. Wu, B. Zhang, P. Gao, A guide to use fluorinated aromatic bulky cations for stable and high-performance 2D/3D perovskite solar cells: The more fluorination the better? *J. Energy Chem.* **64**, 179–189 (2022).
28. J. Zhou, M. Li, S. Wang, L. Tan, Y. Liu, C. Jiang, X. Zhao, L. Ding, C. Yi, 2-CF_3-PEAI to eliminate Pb^0 traps and form a 2D perovskite layer to enhance the performance and stability of perovskite solar cells. *Nano Energy* **95**, 107036 (2022).
29. A. Morteza Najarian, F. Dinic, H. Chen, R. Sabatini, C. Zheng, A. Lough, T. Maris, M. I. Saidaminov, F. P. García de Arquer, O. Voznyy, S. Hoogland, E. H. Sargent, Homomeric chains of intermolecular bonds scaffold octahedral germanium perovskites. *Nature* **620**, 328–335 (2023).
30. M. V. Khenkin, E. A. Katz, A. Abate, G. Bardizza, J. J. Berry, C. Brabec, F. Brunetti, V. Bulović, Q. Burlingame, A. Di Carlo, R. Cheacharoen, Y.-B. Cheng, A. Colsmann, S. Cros, K. Domanski, M. Dusza, C. J. Fell, S. R. Forrest, Y. Galagan, D. Di Girolamo, M. Grätzel, A. Hagfeldt, E. von Hauff, H. Hoppe, J. Kettle, H. Köbler, M. S. Leite, S. Liu, Y.-L. Loo, J. M. Luther, C.-Q. Ma, M. Madsen, M. Manceau, M. Matheron, M. McGehee, R. Meitzner, M. K. Nazeeruddin, A. F. Nogueira, Ç. Odabaşı, A. Osherov, N.-G. Park, M. O. Reese, F. De Rossi, M. Saliba, U. S. Schubert, H. J. Snaith, S. D. Stranks, W. Tress, P. A. Troshin, V. Turkovic, S. Veenstra, I. Visoly-Fisher, A. Walsh, T. Watson, H. Xie, R. Yıldırım, S. M. Zakeeruddin, K. Zhu, M. Lira-Cantu, Consensus statement for stability assessment and reporting for perovskite photovoltaics based on ISOS procedures. *Nat. Energy* **5**, 35–49 (2020).
31. Z. Liang, Y. Zhang, H. Xu, W. Chen, B. Liu, J. Zhang, H. Zhang, Z. Wang, D.-H. Kang, J. Zeng, X. Gao, Q. Wang, H. Hu, H. Zhou, X. Cai, X. Tian, P. Reiss, B. Xu, T. Kirchartz, Z. Xiao, S. Dai, N.-G. Park, J. Ye, X. Pan, Homogenizing out-of-plane cation composition in perovskite solar cells. *Nature* **624**, 557–563 (2023).
32. H. Wang, F. Ye, J. Liang, Y. Liu, X. Hu, S. Zhou, C. Chen, W. Ke, C. Tao, G. Fang, Pre-annealing treatment for high-efficiency perovskite solar cells via sequential deposition. *Joule* **6**, 2869–2884 (2022).

33. Q. Jiang, Z. Chu, P. Wang, X. Yang, H. Liu, Y. Wang, Z. Yin, J. Wu, X. Zhang, J. You, Planar-structure perovskite solar cells with efficiency beyond 21%. *Adv. Mater.* **29**, 1703852 (2017).
34. W. Zhang, S. Pathak, N. Sakai, T. Stergiopoulos, P. K. Nayak, N. K. Noel, A. A. Haghighirad, V. M. Burlakov, D. W. deQuilettes, A. Sadhanala, W. Li, L. Wang, D. S. Ginger, R. H. Friend, H. J. Snaith, Enhanced optoelectronic quality of perovskite thin films with hypophosphorous acid for planar heterojunction solar cells. *Nat. Commun.* **6**, 10030 (2015).
35. D. Luo, W. Yang, Z. Wang, A. Sadhanala, Q. Hu, R. Su, R. Shivanna, G. F. Trindade, J. F. Watts, Z. Xu, T. Liu, K. Chen, F. Ye, P. Wu, L. Zhao, J. Wu, Y. Tu, Y. Zhang, X. Yang, W. Zhang, R. H. Friend, Q. Gong, H. J. Snaith, R. Zhu, Enhanced photovoltage for inverted planar heterojunction perovskite solar cells. *Science* **360**, 1442–1446 (2018).
36. T. J. Jacobsson, J.-P. Correa-Baena, E. Halvani Anaraki, B. Philippe, S. D. Stranks, M. E. F. Bouduban, W. Tress, K. Schenk, J. Teuscher, J.-E. Moser, H. Rensmo, A. Hagfeldt, Unreacted PbI_2 as a double-edged sword for enhancing the performance of perovskite solar cells. *J. Am. Chem. Soc.* **138**, 10331–10343 (2016).
37. J. Liang, X. Hu, C. Wang, C. Liang, C. Chen, M. Xiao, J. Li, C. Tao, G. Xing, R. Yu, W. Ke, G. Fang, Origins and influences of metallic lead in perovskite solar cells. *Joule* **6**, 816–833 (2022).
38. F. A. Stevie, C. L. Donley, Introduction to x-ray photoelectron spectroscopy. *J. Vac. Sci. Technol. A* **38**, 063204 (2020).
39. B. Hu, J. Zhang, Z. Guo, L. Lu, P. Li, M. Chen, C. Li, Manipulating ion migration and interfacial carrier dynamics via amino acid treatment in planar perovskite solar cells. *ACS Appl. Mater. Interfaces* **14**, 15840–15848 (2022).
40. S. M. Park, M. Wei, J. Xu, H. R. Atapattu, F. T. Eickemeyer, K. Darabi, L. Grater, Y. Yang, C. Liu, S. Teale, B. Chen, H. Chen, T. Wang, L. Zeng, A. Maxwell, Z. Wang, K. R. Rao, Z. Cai, S. M. Zakeeruddin, J. T. Pham, C. M. Risko, A. Amassian, M. G. Kanatzidis, K. R. Graham, M. Grätzel, E. H. Sargent, Engineering ligand reactivity enables high-temperature operation of stable perovskite solar cells. *Science* **381**, 209–215 (2023).
41. E. V. Péan, S. Dimitrov, C. S. De Castro, M. L. Davies, Interpreting time-resolved photoluminescence of perovskite materials. *Phys. Chem. Chem. Phys.* **22**, 28345–28358 (2020).
42. J. Chen, S.-G. Kim, N.-G. Park, $FA_{0.88}Cs_{0.12}PbI_3$–(PF_6) interlayer formed by ion exchange reaction between perovskite and hole transporting layer for improving photovoltaic performance and stability. *Adv. Mater.* **30**, e1801948 (2018).
43. S.-C. Yun, S. Ma, H.-C. Kwon, K. Kim, G. Jang, H. Yang, J. Moon, Amino acid salt-driven planar hybrid perovskite solar cells with enhanced humidity stability. *Nano Energy* **59**, 481–491 (2019).
44. B. Guo, R. Lai, S. Jiang, L. Zhou, Z. Ren, Y. Lian, P. Li, X. Cao, S. Xing, Y. Wang, W. Li, C. Zou, M. Chen, Z. Hong, C. Li, B. Zhao, D. Di, Ultrastable near-infrared perovskite light-emitting diodes. *Nat. Photon.* **16**, 637–643 (2022).
45. J. Zhang, B. Hu, Z. Guo, H. Luo, R. Wang, M. Li, M. Chen, C. Li, Zr-metal–organic framework based cross-layer-connection additive for stable halide perovskite solar cells. *Appl. Surf. Sci.* **628**, 157339 (2023).
46. C. Li, A. Guerrero, S. Huettner, J. Bisquert, Unravelling the role of vacancies in lead halide perovskite through electrical switching of photoluminescence. *Nat. Commun.* **9**, 5113 (2018).
47. C. Li, N. Wang, A. Guerrero, Y. Zhong, H. Long, Y. Miao, J. Bisquert, J. Wang, S. Huettner, Understanding the improvement in the stability of a self-assembled multiple-quantum well perovskite light-emitting diode. *J. Phys. Chem. Lett.* **10**, 6857–6864 (2019).
48. Q. Jiang, R. Tirawat, R. A. Kerner, E. A. Gaulding, Y. Xian, X. Wang, J. M. Newkirk, Y. Yan, J. J. Berry, K. Zhu, Towards linking lab and field lifetimes of perovskite solar cells. *Nature* **623**, 313–318 (2023).
49. F. Huang, L. Jiang, A. R. Pascoe, Y. Yan, U. Bach, L. Spiccia, Y.-B. Cheng, Fatigue behavior of planar $CH_3NH_3PbI_3$ perovskite solar cells revealed by light on/off diurnal cycling. *Nano Energy* **27**, 509–514 (2016).
50. M. V. Khenkin, K. M. Anoop, I. Visoly-Fisher, Y. Galagan, F. D. Giacomo, B. R. Patil, G. Sherafatipour, V. Turkovic, H. G. Rubahn, M. Madsen, T. Merckx, G. Uytterhoeven, J. P. A. Bastos, T. Aernouts, F. Brunetti, M. Lira-Cantu, E. A. Katz, Reconsidering figures of merit for performance and stability of perovskite photovoltaics. *Energ. Environ. Sci.* **11**, 739–743 (2018).
51. W. Hui, L. Chao, H. Lu, F. Xia, Q. Wei, Z. Su, T. Niu, L. Tao, B. Du, D. Li, Y. Wang, H. Dong, S. Zuo, B. Li, W. Shi, X. Ran, P. Li, H. Zhang, Z. Wu, C. Ran, L. Song, G. Xing, X. Gao, J. Zhang, Y. Xia, Y. Chen, W. Huang, Stabilizing black-phase formamidinium perovskite formation at room temperature and high humidity. *Science* **371**, 1359–1364 (2021).
52. Q. Jiang, Y. Zhao, X. Zhang, X. Yang, Y. Chen, Z. Chu, Q. Ye, X. Li, Z. Yin, J. You, Surface passivation of perovskite film for efficient solar cells. *Nat. Photon.* **13**, 460–466 (2019).
53. F. Wang, M. Li, Q. Tian, R. Sun, H. Ma, H. Wang, J. Chang, Z. Li, H. Chen, J. Cao, A. Wang, J. Dong, Y. Liu, J. Zhao, Y. Chu, S. Yan, Z. Wu, J. Liu, Y. Li, X. Chen, P. Gao, Y. Sun, T. Liu, W. Liu, R. Li, J. Wang, Y.-B. Cheng, X. Liu, W. Huang, T. Qin, Monolithically-grained perovskite solar cell with Mortise-Tenon structure for charge extraction balance. *Nat. Commun.* **14**, 3216 (2023).
54. Y.-W. Jang, S. Lee, K. M. Yeom, K. Jeong, K. Choi, M. Choi, J. H. Noh, Intact 2D/3D halide junction perovskite solar cells via solid-phase in-plane growth. *Nat. Energy* **6**, 63–71 (2021).
55. W. Yang, B. Ding, Z. Lin, J. Sun, Y. Meng, Y. Ding, J. Sheng, Z. Yang, J. Ye, P. J. Dyson, M. K. Nazeeruddin, Visualizing interfacial energy offset and defects in efficient 2D/3D heterojunction perovskite solar cells and modules. *Adv. Mater.* **35**, e2302071 (2023).
56. D. Gao, R. Li, X. Chen, C. Chen, C. Wang, B. Zhang, M. Li, X. Shang, X. Yu, S. Gong, T. Pauporté, H. Yang, L. Ding, J. Tang, J. Chen, Managing interfacial defects and carriers by synergistic modulation of functional groups and spatial conformation for high-performance perovskite photovoltaics based on vacuum flash method. *Adv. Mater.* **35**, e2301028 (2023).
57. Y. Zhu, P. Lv, M. Hu, S. R. Raga, H. Yin, Y. Zhang, Z. An, Q. Zhu, G. Luo, W. Li, F. Huang, M. Lira-Cantu, Y.-B. Cheng, J. Lu, Synergetic passivation of metal-halide perovskite with fluorinated phenmethylammonium toward efficient solar cells and modules. *Adv. Energy Mater.* **13**, 2203681 (2023).
58. P. Shi, Y. Ding, B. Ding, Q. Xing, T. Kodalle, C. M. Sutter-Fella, I. Yavuz, C. Yao, W. Fan, J. Xu, Y. Tian, D. Gu, K. Zhao, S. Tan, X. Zhang, L. Yao, P. J. Dyson, J. L. Slack, D. Yang, J. Xue, M. K. Nazeeruddin, Y. Yang, R. Wang, Oriented nucleation in formamidinium perovskite for photovoltaics. *Nature* **620**, 323–327 (2023).
59. Q. Feng, X. Huang, Z. Tang, Y. Hou, Q. Chang, S. Nie, F. Cao, X. Niu, J. Yin, J. Li, N. Zheng, B. Wu, Governing PbI_6 octahedral frameworks for high-stability perovskite solar modules. *Energ. Environ. Sci.* **15**, 4404–4413 (2022).
60. S. You, H. Zeng, Y. Liu, B. Han, M. Li, L. Li, X. Zheng, R. Guo, L. Luo, Z. Li, C. Zhang, R. Liu, Y. Zhao, S. Zhang, Q. Peng, T. Wang, Q. Chen, F. T. Eickemeyer, B. Carlsen, S. M. Zakeeruddin, L. Mai, Y. Rong, M. Grätzel, X. Li, Radical polymeric p-doping and grain modulation for stable, efficient perovskite solar modules. *Science* **379**, 288–294 (2023).
61. B. Ding, Y. Ding, J. Peng, J. Romano-deGea, L. E. K. Frederiksen, H. Kanda, O. A. Syzgantseva, M. A. Syzgantseva, J.-N. Audinot, J. Bour, S. Zhang, T. Wirtz, Z. Fei, P. Dörflinger, N. Shibayama, Y. Niu, S. Hu, S. Zhang, F. F. Tiranito, Y. Liu, G.-J. Yang, K. Brooks, L. Hu, S. Kinge, V. Dyakonov, X. Zhang, S. Dai, P. J. Dyson, M. K. Nazeeruddin, Dopant-additive synergism enhances perovskite solar modules. *Nature* **628**, 299–305 (2024).

Acknowledgments: We thank the staff from the BL17B1 beamline of the National Facility for Protein Science in Shanghai (NFPS) at Shanghai Synchrotron Radiation Facility for assistance during data collection. **Funding:** This work was supported by the National Key Research and Development Program (2023YFB3611203), National Natural Science Foundation of China (61974126, 62005230, and 62174141), Natural Science Foundation of Fujian Province of China (no. 2021J06009), and Fundamental Research Funds for the Central Universities (no. 20720210088). **Author contributions:** Conceptualization: Y.Y., M.C., and C.L. Methodology: Y.Y., Q.C., J.Y., and J.L. Investigation: Y.Y., Q.C., J.Y., Y.T., S.J., W.W., S.L., and Y.G. Visualization: Y.Y. Supervision: M.C., K.H., C.L., and R.Z. Writing—original draft: Y.Y. Writing—review and editing: Y.Y., M.C., and C.L. **Competing interests:** The authors declare that they have no competing interests. **Data and materials availability:** All data needed to evaluate the conclusions in the paper are present in the paper and/or the Supplementary Materials.

Submitted 29 March 2024
Accepted 11 December 2024
Published 15 January 2025
10.1126/sciadv.adp3112